Geochemical Perspectives Letters EAG

Tracing anatexis and bottom-up crustal homogenisation with *in-situ* Sm-Nd isotopes

T. Biget, E. Bruand, A. Langone, M. Boyet, A. Caggianelli, P. Bonnand

Supplementary Information

The Supplementary Information includes:

- 1. Sample Selection: *petrographic description of the samples and additional information on the formation ages.*
- 2. Analytical Techniques
- 3. Supplementary Figures S-1 to S-14
- 4. Supplementary Tables S-1 to S-9
- 5. Supplementary Information References

1. Sample Selection

1.1. Petrography

In this section, the samples studied in this contribution are described in detail.

1.1.1. Lower crust samples

Twelve samples were selected from the two units constituting the lower crust of Calabria (Granulite Unit, Metapelite Unit; Table S-1) whose mineral assemblages are described in the section below. Additional data on whole rock and accessory mineral petrography and geochemistry can be found in Biget (2024).

1.1.1.1. Granulite Unit samples

In the Granulite Unit, six samples were studied (four mafic granulites/gabbros and two felsic granulites; Fig. S-1c; Table S-1).

Mafic granulites/Metagabbros

CUR-07 is an amphibole-bearing metagabbro sampled in the Acconia quarry near Curinga (Figs. S-1c; S-2a). It comprises brown hornblende (pargasitic in composition) and plagioclase with minor clinopyroxene (Fig. S-2d), and alternates with coarser-grained hornblendite veins at the cm- to m-scale. This sample is characterised by large (up to 1 mm long), rounded apatite grains, mostly enclosed in amphibole, though some occur at plagioclase-amphibole boundaries or within plagioclase. In CL images, apatite is generally homogeneous but occasionally cross-cut by a complex network of bright veinlets and patches (Fig. S-3a).

CUR-01A and CUR-03 are mafic granulites from the Turrino quarry near Curinga (Figs. S-1c; S-2c,f). CUR-01A is composed of green pargasitic hornblende (~60%) and plagioclase (~35%) with minor clinopyroxene (<2%) and biotite (~1%) grains at hornblende boundaries. Accessory minerals include apatite, ilmenite, and rare zircon. CUR-03 is composed of plagioclase (~65%), orthopyroxene (~15%), biotite (~8%), with minor K-feldspar (<5%), clinopyroxene, sulfides, and quartz. Apatite, ilmenite, allanite, and zircon are the main accessory phases. In this sample, only allanite has been analysed and characterised. This mineral, up to 300 µm long, is found in association with orthopyroxene or enclosed in biotite and shows either homogeneous, patchy, or sector zoning in BSE (Fig. S-3b).

ZAP-11 is a mafic granulite sampled near the locality of Zappaterra. It consists of plagioclase (~60%), green pargasitic hornblende (~25%), clinopyroxene (~10%), orthopyroxene (~4%) and minor biotite (± quartz and K-feldspar) with ilmenite, apatite, and zircon as the main accessory phases. Numerous Fe-oxide grains are also present.

Felsic granulites

CUR-05 is a felsic granulite that occurs as lenses in metagabbros and hornblendites of the Acconia quarry (north of the Serre Massif), which is crossed by the Curinga-Girifalco Line fault (Fig. S-2a,b,e). Its mineralogical assemblage is composed of plagioclase, garnet, quartz, biotite ± K-feldspar. Plagioclase (55%) and garnet (35%) are the dominant minerals, and accessory minerals are, in order of decreasing abundance, rutile (~1%), monazite, zircon, and rare apatite grains. Garnet grains are often grouped into mm- to cm-sized aggregates surrounded by quartz–feldspar matrix. They are highly fractured, commonly associated with Fe-oxide, and contain inclusions of plagioclase, quartz, and biotite, as well as accessories such as rutile, apatite (± monazite and zircon). Biotite is highly deformed and sometimes chloritised and its modal abundance is generally very low (<2%). Epidote is found in altered matrix zones.

CUR-02, another felsic granulite, was sampled from tectonic boudins in contact with mafic granulites in the Turrino quarry near Curinga (Fig. S-2c,g). Its modal mineralogical composition differs substantially from the previous sample, and consists of plagioclase (33%), quartz (30%), K-feldspar (19%), garnet (13%), and biotite (5%). In this sample, garnet grains are smaller (<1 mm) and contain some inclusions of quartz and plagioclase. Biotite is more abundant than in CUR-05. The main accessory minerals are, in order of decreasing abundance, rutile, ilmenite, apatite, zircon, and monazite.

In felsic granulites, monazite grains are generally small (<30 µm) and mainly located in the matrix. In CUR-02, some larger grains, up to 100 µm, can nevertheless be found as inclusions in garnet, mainly at its rim or in association with apatite. In CUR-05, monazite grains are occasionally rimmed by epidote-allanite coronas. In BSE, most monazite grains from both samples appear unzoned (Fig. S-4), though rare core–rim zoning with Th-rich rims is observed in CUR-02 (Fig. S-4).

1.1.1.2. Metapelite Unit samples

Six migmatitic paragneisses derived from pelitic to psammitic protoliths were sampled along a north-south transect through the Metapelite Unit (Fig. S-1c; Table S-1). This transect is characterised by a temperature gradient ranging from ~850 °C at the base of the unit to ~650-700 °C at the top (Schenk, 1984; 1990; Acquafredda *et al.*, 2006; 2008; Fornelli *et al.*, 2012; Festa *et al.*, 2024). As already noted by previous studies (*e.g.*, Caggianelli *et al.*, 1991; Fornelli *et al.*, 2002), the deepest rocks present a very restitic appearance with a quantity of leucosome gradually increasing towards the top of the unit.

AMA-43 is the deepest and most restitic sample. It contains large (up to 10 cm) garnet crystals wrapped by mesosomes defining the main foliation and includes large and prismatic sillimanite, biotite flakes as well as minor quartz and K-feldspar (Fig. S-5a). Garnet is marked by a fairly pronounced alteration at its edges, which tends to penetrate the grain interior along the fractures, forming zones enriched in iron oxide and clay minerals such as kaolinite. Mineral inclusions identified in these garnet grains include quartz, biotite, sillimanite, ilmenite, rutile, zircon, and monazite. A recent study showed that these large garnets formed by the coalescence of peritectic crystals during the migration of melt in pull-apart structures which subsequently clogged the melt extraction channels (Festa *et al.*, 2024). At the interface between garnet and the mesosome, a small volume of leucosome, composed mainly of quartz and K-feldspar, can be found with rare occurrences of biotite, garnet, and sillimanite. Accessory minerals are rutile, ilmenite, monazite, and zircon, which are essentially located in the mesosome. In this sample, most monazite grains are observed in the mesosome, associated with biotite or sillimanite, or as inclusions in garnet, while rare grains are present in the leucosome. Their sizes are generally much larger than those found in felsic granulites, with some grains reaching up to 200 µm. In this sample, monazite is generally relatively homogeneous on the BSE images, except for rare grains showing Th-rich and LREE-poor rims (Fig. S-4).

MROS-13D is a composite gneiss composed of metasedimentary (psammitic) layers interbedded with sub-concordant cm-thick orthopyroxene-bearing layers (Fig. S-5b). In thin section, this rock shows pronounced mineralogical contrasts between the metapsammitic layers composed of biotite, garnet, plagioclase, and quartz and the orthopyroxene-bearing layers that exhibit an orthopyroxene–garnet–plagioclase–quartz mineralogical assemblage. Accessory phases also differ between the two lithologies. The metapsammitic layers include rutile, ilmenite, zircon, and monazite (up to 150 µm), while the orthopyroxene-bearing layers contain ilmenite, apatite, and zircon. Although rare, small monazite grains (<50 µm) are also observed in this lithology (Fig. 2, main text). Notably, some monazite grains at the interface between the two lithological domains show distinct core–rim zoning with BSE-bright rims enriched in Th (Figs. 2, main text; S-4).

MROS-13A is a migmatitic metapsammitic gneiss sampled approximately 3 m away from MROS-13D whose mineralogy closely matches that of the metasedimentary layers of the composite gneiss, consisting mainly of quartz, plagioclase, biotite, and garnet.

MROS-16 is a migmatitic paragneiss of semipelitic composition. The mesosome, defining the foliation, comprises quartz, plagioclase, biotite, sillimanite, and garnet, while the leucosome consists of quartz, plagioclase, and K-feldspar with abundant garnet and minor biotite and sillimanite. Accessory minerals include rutile, ilmenite, monazite, and zircon. Monazite grains occur both in the quartz-feldspathic matrix and as inclusions within garnet, with sizes reaching up to 100 µm. As in AMA-43, most monazite grains appear homogeneous in BSE (Fig. S-4), although a few show patchy zoning or core–rim zoning, with Th-enriched rims.

CAP-19 and SNIC-20A are migmatitic paragneisses derived from pelitic protoliths. Macroscopically, both display concordant leucosomes aligned with the foliation (stromatic migmatites from the nomenclature of Sawyer (2008); Fig. S-5c,d). CAP-19 comprises biotite (10–15%)–garnet–prismatic sillimanite–cordierite (± quartz ± plagioclase) mesosomes, along with quartz–plagioclase–K-feldspar leucosomes. The accessory phases, in order of decreasing abundance, are rutile, monazite, zircon, and apatite. SNIC-20A shows a similar mineralogy but lacks K-feldspar. Its accessory minerals include apatite, rare xenotime and rutile, which is partially replaced by ilmenite. In this sample, biotite is more abundant, comprising up to 30% of the mesosome. Monazite grains in both samples are typically located in mesosomes, associated with biotite or sillimanite. They range from large grains (100–150 µm) to smaller ones (<50 µm) included in garnet. In BSE images, CAP-19 monazite often exhibits complex internal patchy zoning with Th- and Y-rich domains (Fig. S-4). Monazite from SNIC-20A displays complex patchy or core–rim zoning with irregular Y-rich rims and a porosity network, consistent with coupled dissolution–reprecipitation processes (*e.g.*, Varga *et al.*, 2020; Fig. S-4).

1.1.2. Migmatitic Border Zone samples

1.1.2.1. Migmatites

One migmatitic paragneiss (PETRI-51) was sampled in a quarry near Petrizzi, very close to the contact between the top of the Metapelite Unit and the Migmatitic Border Zone (Figs. S-1c; S-6a). Its mineralogy closely resembles that of SNIC-20A with abundant biotite and large crystals of cordierite, particularly visible at outcrop (Fig. S-6b). This sample is also characterised by the presence of carbonate (siderite) and andalusite as partial replacement products of cordierite. This type of reaction (Crd + CO_2 → Carb + And/Ky + Qz) has already been observed in these shallow samples from the Metapelite Unit (Schenk, 1990) as well as in other amphibolite- to granulite-facies metapelites worldwide (*e.g.*, Ellis and Hiroi, 1997). In Calabria, it was interpreted as a record of isobaric cooling at P <4 kbar following the peak of metamorphism (Schenk, 1990). Accessory minerals include monazite, zircon, and ilmenite, with rare apatite and rutile. Monazite is mostly found in the mesosome and commonly shows strong core–rim zoning with Y-rich rims, while other grains are more homogeneous in BSE (Fig. S-4). Another migmatite (diatexite) was sampled in the Vallelonga quarry (VAL-27A/B). The mesosome is represented by a garnet–biotite gneiss (VAL-27A), composed of biotite, quartz, plagioclase, and garnet, with foliation defined by biotite. This gneiss is pervasively intruded by trondhjemitic–tonalitic melts (VAL-27B; Fig. S-7c), consisting of quartz, plagioclase, and garnet that constitute the leucosome. Some of these leucosomes are isoclinally folded on the cm- to dm-scale, a common feature in the Serre Massif (Schenk, 1984), which indicates deformation subsequent to their formation. Accessory minerals in VAL-27A include ilmenite, monazite, zircon, and rare apatite, whereas VAL-27B contains ilmenite, zircon, and exceptionally large monazite grains (up to 500 µm in thin section), displaying complex core–rim, patchy, or oscillatory zoning (Fig. S-8a).

1.1.2.2. Igneous rocks

In this zone, a large diversity of igneous rocks crop out. Samples VAL-22, VAL-23 and VAL-30 were collected from complex outcrops in the Vallelonga quarry (Figs. S-1a; S-7a–f). They consist of: strongly foliated garnet-bearing tonalite (VAL-22), monzogranite (VAL-23) and strongly foliated cummingtonite-bearing mafic rock occurring as a dm-sized lens (VAL-30). Two other samples from the MBZ were collected between Gasperina and Montauro localities: (i) an amphibole-bearing mafic rock (GASP-55; Fig. S-7g) and (ii) a foliated garnet-bearing tonalite (MPAO-58) sampled 1 km west of Montepaone (Figs. S-1c; S-7h).

VAL-22 is a strongly foliated garnet-amphibole tonalite at the contact with the garnet-biotite gneiss (Fig. S-7d). This rock is composed of biotite (defining the foliation), plagioclase, quartz, hornblende (developing around cummingtonite cores), and garnet. Accessory phases are allanite (up to 300 μm, with dark cores and bright rims; Fig. S-8e), apatite (up to 400 μm, homogeneous in CL), zircon, and rare patchy-zoned monazite.

VAL-23 is a sheared K-feldspar–quartz–plagioclase monzogranite, which intrudes the main garnet-biotite gneiss body (Fig. S-7e). Accessory minerals are ilmenite, monazite, zircon, and apatite. Monazite grains can reach exceptionally large sizes (up to 500 μm in thin section) and exhibit oscillatory or patchy zoning (Fig. S-8b), similar to VAL-27A.

VAL-30 is a strongly foliated cummingtonite-bearing mafic rock, composed of abundant plagioclase (>50%), biotite, aggregates of cummingtonite commonly occurring at plagioclase joints and texturally associated to orthopyroxene, and minor quartz. Accessory minerals include ilmenite, apatite, allanite, and rare zircon (Fig. S-7f). Apatite (up to 400 μm) and allanite (up to 200 μm) are texturally related to biotite and cummingtonite (as inclusions or at their edges). Apatite is unzoned in CL, while allanite shows either a bright core–dark rim zoning or is relatively homogeneous in BSE (Fig. S-8c).

GASP-55 is a hybrid amphibole-bearing mafic rock that displays cm-sized gabbroic remnants (Fig. S-7g). It contains plagioclase (>50%), green hornblende (magnesio-hornblende to pargasite), cummingtonite aggregates, and minor biotite and quartz. Accessory minerals are ilmenite, apatite, zircon, and allanite, in order of decreasing abundance. Apatite (up to 400 μm) is mostly enclosed or at the edges of hornblende and cummingtonite and shows variable CL zoning from core–rim (with a dark core surrounded by a bright rim) to more homogeneous textures (Fig. S-8d). Allanite is scarce in thin section and is almost homogeneous in BSE (Fig. S-8d).

MPAO-58 is a foliated garnet-bearing tonalite composed of feldspar, quartz, biotite (defining the foliation), and garnet (Fig. S-7h) with minor chlorite replacing biotite. Accessory minerals include ilmenite, apatite, zircon, and opaques. Apatite occurs as crystals (up to 400–500 μm) mainly associated with biotite, although some grains can also be found in quartz or feldspar (Fig. S-8f). In CL images, apatite can be homogeneous or exhibit a clear bright-to-dark rimward zoning (Fig. S-8f). A few grains show core–rim zoning with dark cores and bright rims (*e.g.*, grain #54; Fig. S-8f).

1.1.3. Middle crust granitoids samples

1.1.3.1. Samples selection

Six granitoid samples representing the main magmatic units of the Serre batholith were selected (Table S-2). For the tonalite unit, we sampled one foliated tonalite at the western extremity of Montepaone village (MPAO-56; Fig. S-1c) and one foliated amphibole-bearing tonalite approximately 2 km south of Squillace (SQUI-54; Fig. S-1c). In these localities, the granitoids are moderately to strongly foliated with the presence of mm- to dm-sized stretched Microgranular Mafic Enclaves (MME). They represent the deepest and oldest granitoids of the Serre batholith (*e.g.*, Caggianelli *et al.*, 2000; Fiannacca *et al.*, 2017). An unfoliated amphibole-bearing tonalite (CAPO-39) was also collected in the Capo Vaticano Promontory (CVP) area (Fig. S-1a). Two samples from the two-mica granite/granodiorite unit were selected; one belonging to the porphyritic facies, characterised by cm-sized K-feldspar megacrysts, sampled near Parghelia beach at the CVP (PAR-76; Fig. S-1a) and a two-mica equigranular granite collected ~2 km east of Satriano in the Serre Massif (SAT-62; Fig. S-1c). Finally, a granodiorite from the uppermost and youngest magmatic unit was collected (STIL-63; Fig. 1c). This sample comes from the top of the granitic body, 5 km west of Stilo near the contact-metamorphic aureole affecting the Stilo-Pazzano phyllites (Fig. S-1a; Festa *et al.*, 2013). These outcrops also contain globular MME.

1.1.3.2. Mineral assemblages

In the following, a detailed petrographic description of the selected granitoids is provided. Their mineralogical assemblages are summarised in Table S-2.

(Amphibole) tonalites

MPAO-56 and SQUI-54 are two medium- to coarse-grained tonalites showing a moderate to strong foliation (Fig. 9a). They display a hypidiomorphic texture with, in order of decreasing abundance, unzoned to weakly zoned euhedral to subhedral plagioclase, subhedral biotite, and anhedral quartz (Table S-2). SQUI-54 also includes subhedral green hornblende. Their main accessory minerals are apatite, zircon, allanite, and titanite with modal proportions varying from one sample to another. Apatite is present in both samples, typically associated with biotite (or amphibole) and less frequently with quartz or plagioclase. Grains reach 300–350 µm and display oscillatory or, less commonly, core–rim zoning in CL (Fig. S-10a,c). Tiny zircon grains included in apatite are frequent, especially at the interface between dark and bright domains (*e.g.*, grain #04 in MPAO-56; Fig. S-10a). Titanite is rarely present in MPAO-56 and common in SQUI-54, reaching up to 400 µm. It is consistently associated with biotite or amphibole at grain edges or within cleavages and is generally homogeneous in BSE, though patchy zoning can occur (Fig. S-10c). Allanite, found in both samples, occurs as large (up to 400 µm) crystals often rimmed by epidote and associated with biotite or amphibole. BSE textures range from homogeneous to sector and patchy zoning (Fig. S-10a,c).

CAPO-39 is an amphibole-bearing tonalite composed of plagioclase, quartz, biotite, and K-feldspar with minor amphibole, chlorite and secondary epidote (Table S-2). Apatite, titanite, and zircon are the main accessory minerals. Apatite grains are up to 300–400 µm long and are typically associated with biotite and less commonly enclosed in quartz or plagioclase. In CL images, most grains show pronounced oscillatory zoning (S-10b). Less commonly, grains display core–rim zoning with a dark, unzoned core and a bright, oscillatory-zoned rim. These zones are separated by irregular interfaces suggesting a dissolution–

reprecipitation process. (*e.g.*, grain #10; Fig. S-10b). Titanite typically occurs as small (<50 µm), anhedral crystals located within biotite cleavages, although larger subhedral grains, up to 300 µm, are also present. In BSE images, titanite appears homogeneous (Fig. S-10b).

Two-mica (porphyritic) granodiorites and granites

The two-mica granodiorite PAR-76 is medium to coarse grained and shows a porphyritic texture with cm-sized K-feldspar megacrysts commonly aligned by magmatic flow. The matrix consists of euhedral to subhedral weakly zoned plagioclase, subhedral to anhedral K-feldspar (microcline), anhedral quartz, euhedral biotite, and subhedral to anhedral muscovite (Fig. 9b; Table S-2). Accessory minerals include zircon, ilmenite, apatite, monazite, titanite, and secondary allanite. Apatite (up to 200 µm) is commonly associated with biotite, muscovite, and K-feldspar megacrysts, and less frequently with plagioclase and quartz. CL images show mostly homogeneous textures with common inclusions of tiny monazite and zircon (<20 µm; Fig. S-11a). Monazite (up to 50 µm) occurs within K-feldspar megacrysts or matrix minerals, mainly alongside biotite, and often displays weak zoning in BSE (Fig. S-11a). Complex intergrowths of apatite, monazite, allanite, zircon, and ilmenite are common (Fig. S-11a1–3). Evidence of monazite breakdown into apatite + allanite suggests a low-grade metamorphic overprint or metasomatic influence (*e.g.*, Schulz, 2021; Fig. S-11a2,3).

Sample SAT-62 is a medium-grained, isotropic, equigranular two-mica granite with a hypidiomorphic texture consisting of anhedral to subhedral weakly zoned plagioclase, anhedral quartz, subhedral K-feldspar, and muscovite/biotite plates. Accessory minerals include apatite, ilmenite, zircon, and monazite with minor xenotime, secondary allanite, and titanite (Table S-2). Apatite occurs as small crystals (<50 µm), enclosed in plagioclase and K-feldspar, and could not be separated for analysis. Monazite grains (up to 100 µm) are either homogeneous or display patchy and sector zoning (Fig. S-11b).

Biotite granodiorite

STIL-63 is a medium-grained isotropic granodiorite showing a hypidiomorphic texture and composed of plagioclase, quartz, biotite, and K-feldspar by order of decreasing modal abundance (Fig. 9c; Table S-2). Plagioclase is commonly sericitized and biotite is sometimes altered to chlorite. Accessory minerals include ilmenite, apatite, and zircon with rare allanite and titanite.

Only apatite was characterised in this sample. Grains are enclosed within or located at biotite edges and less commonly in plagioclase and quartz and can reach 400 µm in size (Fig. S-12). In CL images, apatite is homogeneous or shows weak oscillatory zoning. Most grains are cross-cut by a complex network of bright veinlets and patches (Fig. S-12). A few grains display dark core–bright rim zoning (*e.g.*, grain #11 in STIL-63; Fig. S-12).

1.2. Ages of the formations

The protoliths of the paragneisses and felsic granulites are inferred to derive from arenite–pelite sequences deposited during the Neoproterozoic (Schenk, 1990; Fornelli *et al.*, 2020). U–Pb dating of monazites from the lower-crustal samples analysed in this study yields mostly concordant dates between 270 and 300 Ma, with a peak at 290 Ma in the Kernel Density Estimation (KDE) diagram, corresponding to the late Variscan magmatic event (Fig. S-13; Biget, 2024). Monazites analysed for Sm–Nd isotopes in this study all fall within this age range. Approximately 10% of the dates exceed 325 Ma, likely reflecting prograde monazite growth or inherited monazites, whereas ~10% are younger than 270 Ma, possibly recording later geological events that remain poorly constrained, potentially related to the opening of the Tethys Ocean or pre-Alpine tectono-metamorphic activity (Biget, 2024). The emplacement ages of lower-crustal metagabbros and mafic granulite protoliths remain poorly constrained and debated, potentially ranging from Ediacaran to Cambrian, although some intrusions of Variscan age are also possible (e.g., Schenk, 1980; Caggianelli *et al.*, 2013; Fiannacca *et al.*, 2024). Despite these uncertainties regarding the timing of the intrusions, all εNd values of the mafic rocks in this study were recalculated at 290 Ma, corresponding to the end of the regional metamorphic peak in Calabria. By contrast, granitoid emplacement ages are generally well constrained, occurring between 306.4 ± 1.6 to 295.0 ± 1.4 Ma (Langone *et al.*, 2014) or 297.3 ± 3.1 to 292.2 ± 2.6 Ma (Fiannacca *et al.*, 2017). Sm–Nd isochrons from some samples of this study also yield dates of the same range, albeit with larger uncertainties (Biget, 2024).

2. Analytical techniques

2.1. Whole rock Sm-Nd analyses

Whole rock Sm-Nd analyses (Table S-3) were carried out at the Geo-Océan laboratory (Pôle Spectrométrie Océan-IUEM) at Brest. The Nd separation protocol is derived from Pin *et al.* (1994) and Chauvel *et al.* (2010). 1.5 mL of the sample stock solution (HCl 2.5 N) was loaded into the BioRad AG 50-X8 cationic resin in order to isolate the REE. This REE fraction was then taken up with HCl 0.2 N and processed through the Ln Spec resin columns to collect Nd. The monoelemental fraction of Nd obtained after column separation was diluted into 1 to 6 µL of HCl 1 N (variable according to the amount of Nd collected). 1 µL of this solution was then pipetted on a Re filament (99.95% purity). The Nd isotope analyses were performed in dynamic mode on the IUEM ThermoScientific Triton® TIMS usingdouble Re filaments. Each run consisted of 20 blocks × 10 cycles (8.389-s integration time per line) with a 30-s baseline measurement every block. Isotopic ratios were mass-fractionation-corrected using an exponential law with $^{146}Nd/^{144}Nd$ = 0.7219. Repeated measurements of the JNDi-1 reference material gave $^{143}Nd/^{144}Nd$ = 0.512094 ± 15 (2SD, n = 9) and are consistent with the value of 0.512099 ± 5 measured using a dynamic routine (Garçon *et al.*, 2018). AGV-2 and BHVO-2 gave respectively $^{143}Nd/^{144}Nd$ = 0.512767 ± 5 (2SE) and 0.512996 ± 5 (2SE) and are consistent with published values reported in the GeoReM database ($^{143}Nd/^{144}Nd$ = 0.512786 ± 14 for AGV-2 and 0.512979 ± 14 for BHVO-2).

2.2. In situ analyses

This section details the imaging and *in situ* analyses performed on the studied samples and relevant for this study.

Monazite analyses from all samples and allanite analyses from CUR-03, VAL-30 and GASP-55 were acquired on polished thin sections, whereas apatite and titanite for all samples as well as allanite grains from MPAO-56 and SQUI-54 were analysed on epoxy mounts. These grains were separated using conventional magnetic and density separation techniques, mounted on Epoxy resin discs, and polished for *in situ* analyses.

2.2.1 Image acquisition

BSE images were acquired using a Scanning Electron Microscope (SEM) Thermofisher (formerly FEI) QUANTA 200 with an accelerating voltage of 20 keV equipped with an EDS Oxford XMAX 80 detector in Brest, France. Thin sections and accessory mineral images were processed using the Oxford Aztec software and accessory phases were identified using the "Particle mode". Cathodoluminescence images of apatite were obtained with a KeDev Centaurus CL detector housed on a JEOL JSM-5910LV SEM (accelerating voltage: 15 keV) at the Laboratoire Magmas et Volcans (LMV) in Clermont-Ferrand, France.

2.2.2 Electron Probe Microanalyses (EPMA)

Quantitative chemical analyses for apatite were carried out using the CAMECA SX 100 microprobe from the Microsonde Ouest laboratory (Brest, France) with an accelerating voltage of 20 keV and a beam current of 40 nA. LLIF crystal was used for Mn and Nd, TAP for Na, Si and Y, PET for P and Ca, PC1 for F and LPET for Cl and S. Kα X-ray line was used for Cl, P, Ca, S, Mn, F, Na and Si, while Lα X-ray line was used for Y and Nd. Durango was used as a standard for quality control (Table S-7). A defocused beam of 10 µm was applied to avoid migration effects described for halogens (F, Cl; Pyle *et al.*, 2002). Peak and background counting time for all elements are provided in Table S-7.

2.2.3. In situ Sm-Nd analyses

In situ analyses were conducted on all samples except for three lower crust samples (CUR-01A, ZAP-11 and MROS-13A). Detailed results are provided in Table S-4. Monazite, apatite, and allanite *in situ* Sm-Nd analyses were performed during three sessions on the LMV Thermo Fisher Scientific™ Neptune Plus™ mass spectrometer coupled with the 193 nm Resonetics Resolution M-50E laser following the protocol described in Doucelance *et al.* (2020). Titanite analyses were acquired at the Geo-Océan laboratory (Pôle Spectrométrie Océan-IUEM) at Brest on a Thermo Fisher Scientific™ Neptune Plus™ mass spectrometer coupled with a COMPexPro 193 nm Excimer laser (GeoLas HD system). The first 20 cycles of every measurement were used to evaluate the baseline level of each Faraday cup. Analyses usually consisted of 90 measurement cycles. Depending on the run, a spot size of 12, 15 or 20 µm was used for monazite; 20 or 33 µm for allanite; 120 µm for titanite; and 133, 120 or 107 µm for apatite. Rasters (120 * 80 µm or 117 * 93 µm) were also performed on apatite to minimise analytical uncertainties. For thin sections, the laser frequency was set to 4 Hz and the fluence to 3.0-3.4 J/cm^2. For grains analysed on mounts, frequency was increased to 6 Hz with similar fluence. For titanite analysed with the GeoLas system, the frequency was set to 8 Hz and the fluence to 12 J/cm^2. Helium flow rate was 700-800 ml/min while N_2 flow rate varied between 2.3 and 8.5 ml/min, depending on session conditions. The oxide level (ThO^+/Th) at the beginning of the session was minimised to avoid a ^{145}Nd/^{144}Nd drift, as described by Fisher *et al.* (2020) and Doucelance *et al.* (2020). JNdi-1 doped glass was analysed regularly during the sessions to monitor potential instrumental drift (Fisher *et al.*, 2011; Doucelance *et al.*, 2020). Primary standards STK for monazite (^{143}Nd/^{144}Nd = 0.511895; Fisher *et al.*, 2020), Durango for apatite (^{143}Nd/^{144}Nd = 0.512473; Doucelance *et al.*, 2020), Connecticut for allanite (^{143}Nd/^{144}Nd = 0.512106; Wang *et al.*, 2022), and MKED-1 for titanite (^{143}Nd/^{144}Nd = 0.511630; Spandler *et al.*, 2016) were analysed regularly under the same conditions as the unknowns and were used for normalisation and instrumental drift correction when necessary (Tables S-5). Gale allanite (^{143}Nd/^{144}Nd = 0.512999; Wang *et al.*, 2022), Tory Hill apatite (^{143}Nd/^{144}Nd = 0.512048; Fisher *et al.*, 2020), and Khan titanite (^{143}Nd/^{144}Nd = 0.511632; Xu *et al.*, 2018) were used as secondary standards for quality control (Tables S-6). A value of ^{145}Nd/^{144}Nd = 0.348415 (Wasserburg *et al.*, 1981) was used as a reference for internal quality control of the analyses. Isotopic ratio calculations were performed off-line using an in-house Microsoft Excel™ spreadsheet. The $\varepsilon Nd_{(i)}$ were calculated using the decay constant $\lambda = 6.54.10^{-12}$ s^{-1} (Lugmair and Marti, 1978) and CHUR parameters from Bouvier *et al.* (2008). Error propagations on the $\varepsilon Nd_{(i)}$ were carried out using the spreadsheet from Ickert (2013).

2.2.4. Laser ablation inductively coupled plasma mass spectrometry (LA-ICP-MS)

Trace elements of GASP-55 apatite (Table S-8) were analysed by LA-ICP-MS using the Thermo Element XR linked with a COMPexPro 193 nm Excimer laser (GeoLas HD system) at Geo-Océan laboratory (Pôle Spectrométrie Océan-IUEM) at Brest. Each analysis consisted of 25 s of background acquisition and 85 s of ablation using spot sizes of 32 or 24 µm, a 5 Hz repetition rate, and a laser fluence of 15 J/cm^2. Elemental concentrations were calculated using a sample bracketing method, with NIST-610 (Jochum *et al.*, 2005) as the primary standard to calculate elemental concentrations and to correct instrumental drift. ^{43}Ca concentration, previously measured by EPMA, served as the internal standard for data normalisation. To ensure data quality, USGS glass NIST-612 (Jochum *et al.*, 2005) and standard Durango apatite (Marks *et al.*, 2012) were regularly analysed under identical conditions (Table S-9). Data were processed using GLITTER® software (Van Achterbergh *et al.*, 2001; Griffin *et al.*, 2008).

3. Supplementary Figures

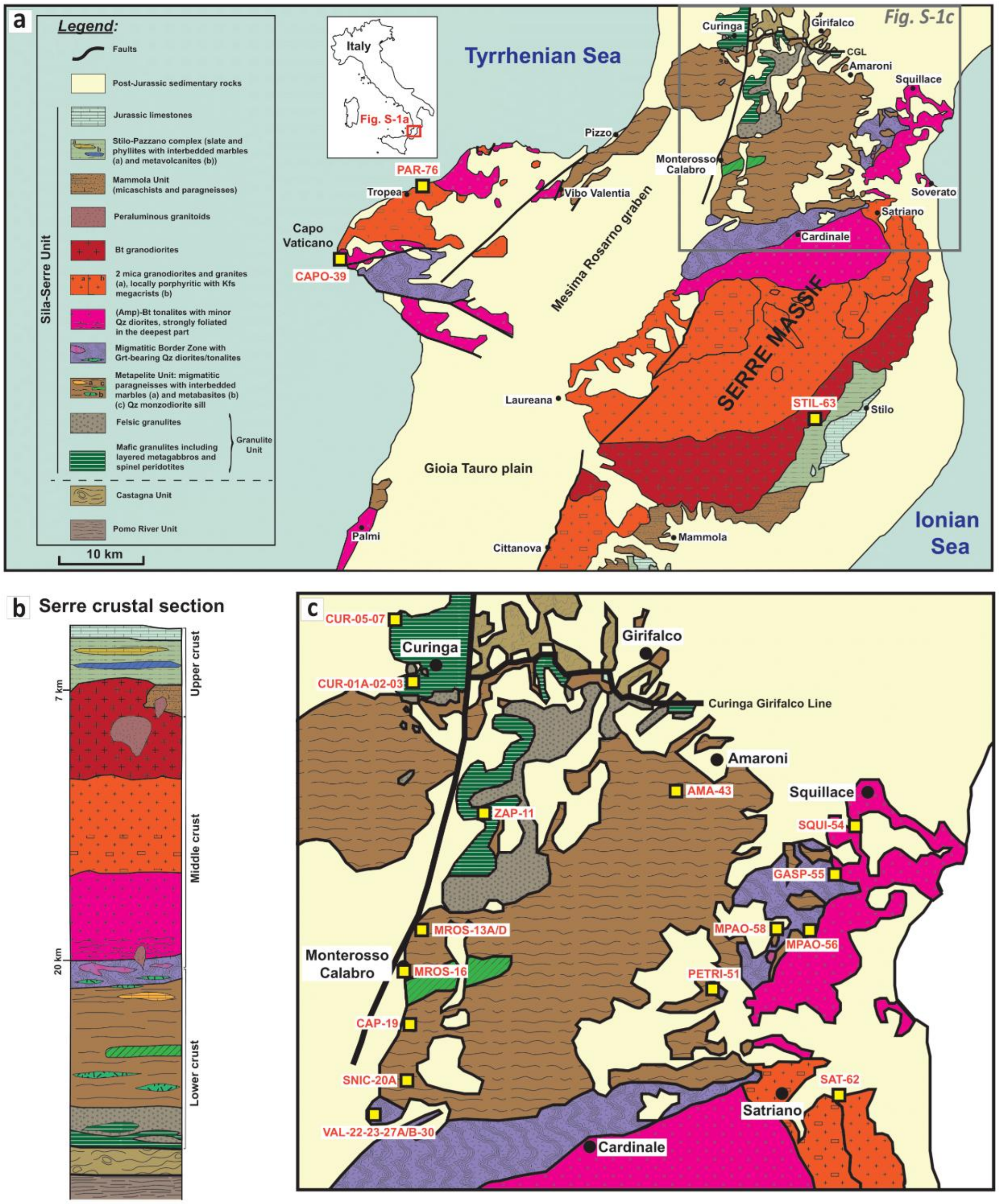

Figure S-1 **(a)** Simplified geological sketch map of the Serre Massif-Capo Vaticano area (modified from Caggianelli *et al.*, 2013 and Fiannacca *et al.*, 2015). **(b)** Schematic lithological column for the Serre Massif (modified from Festa *et al.*, 2004 and Caggianelli *et al.*, 2013). **(c)** Overview of the lower crust with location of the selected samples.

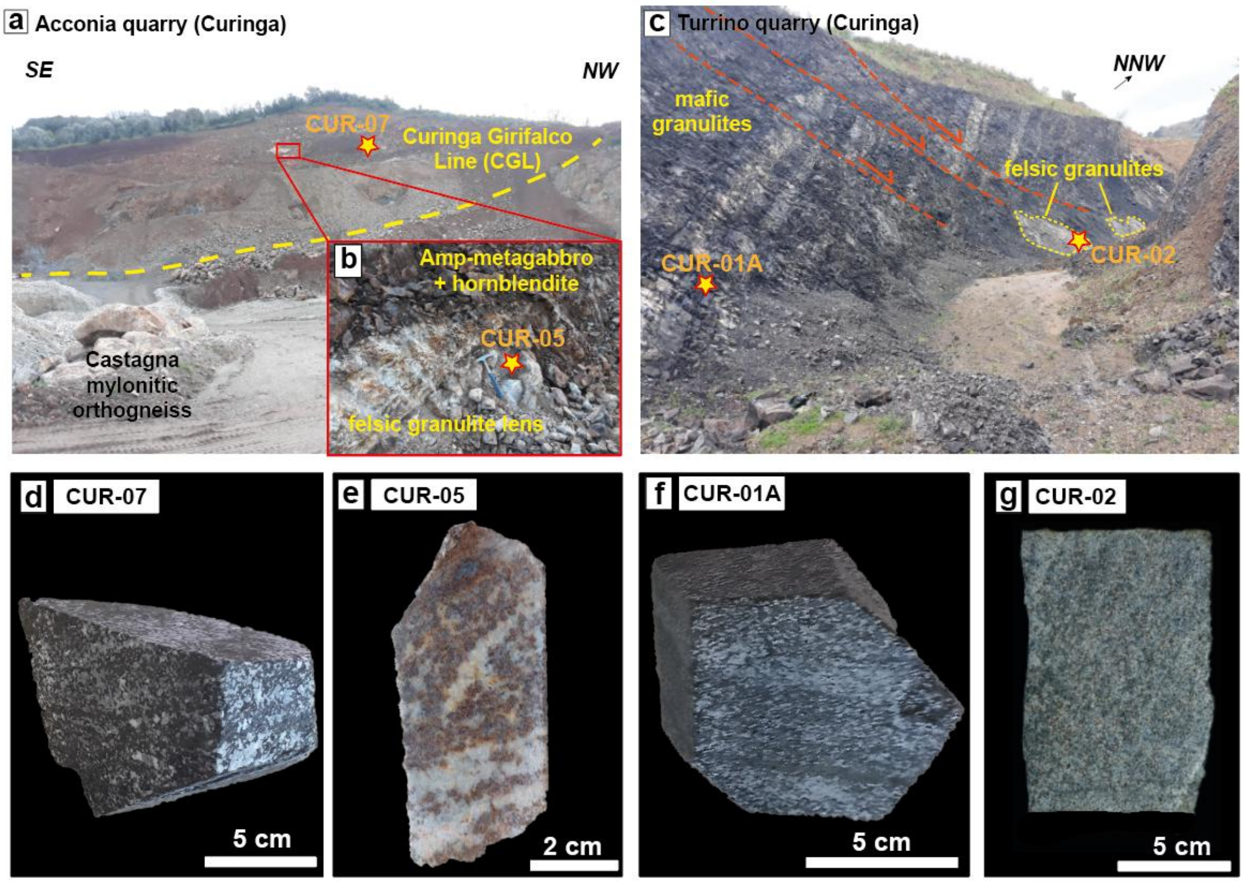

Figure S-2 Outcrop and macroscopic views of some of the selected samples from the Granulite Unit. **(a)** Overview of the Acconia quarry near Curinga, transected by the Curinga-Girifalco Line (CGL) fault (*e.g.*, Brandt and Schenk, 2020; Festa *et al.*, 2020), and showing lenses of felsic granulite (CUR-05) embedded in amphibole metagabbro (CUR-07) and hornblendite **(b)**. **(c)** Overview of the front of the Turrino quarry, cross-cut by normal faults and displaying mafic granulite (CUR-01A) and tectonic boudins of felsic granulite (CUR-02). **(d-g)** Macroscopic view of CUR-07 amphibole metagabbro, CUR-05 felsic granulite, CUR-01A mafic granulite and CUR-02 felsic granulite.

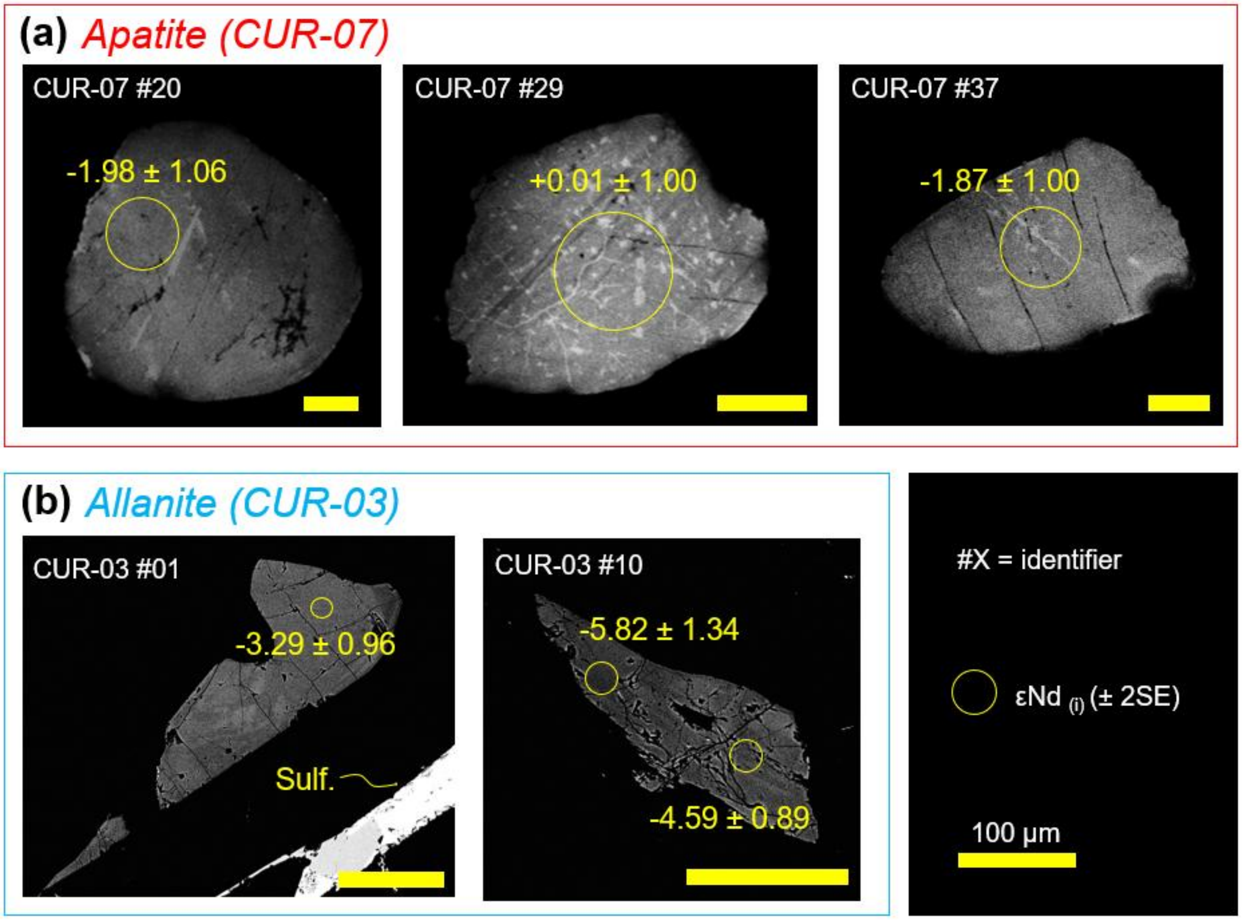

Figure S-3 Representative CL images of apatite from CUR-07 metagabbro **(a)** and BSE images of allanite from CUR-03 mafic granulite **(b)**. The yellow circles indicate the position of the laser spots for Sm-Nd isotopic analyses. εNd were calculated at 290 Ma for CUR-07 apatite and CUR-03 allanite. The yellow scale bar is 100 µm.

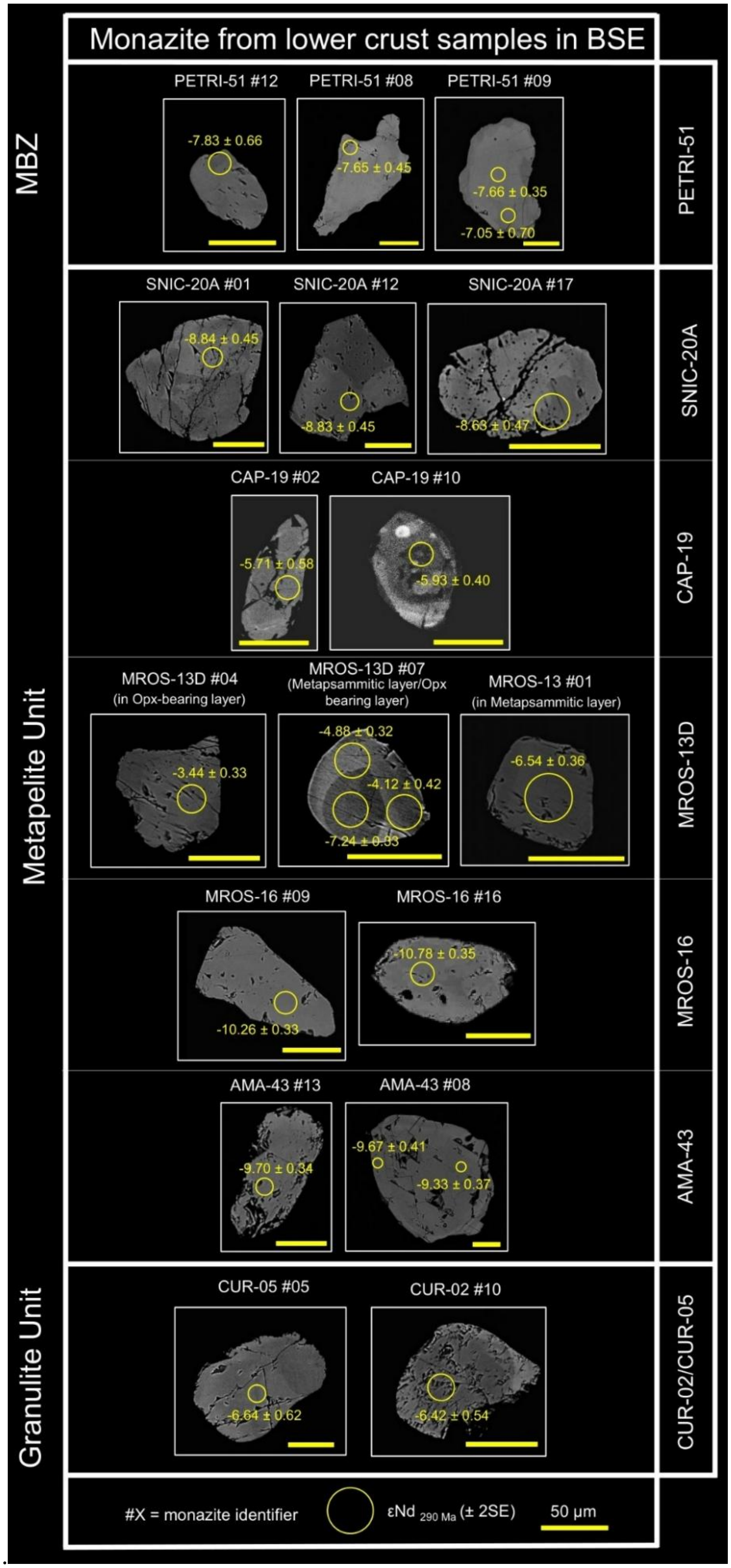

Figure S-4 Representative BSE images of monazite from the samples investigated in this study. The yellow circles indicate the position of the laser spots for Sm-Nd isotopic analyses. εNd were calculated at 290 Ma and uncertainties are ± 2SE. The yellow scale bar is 50 µm.

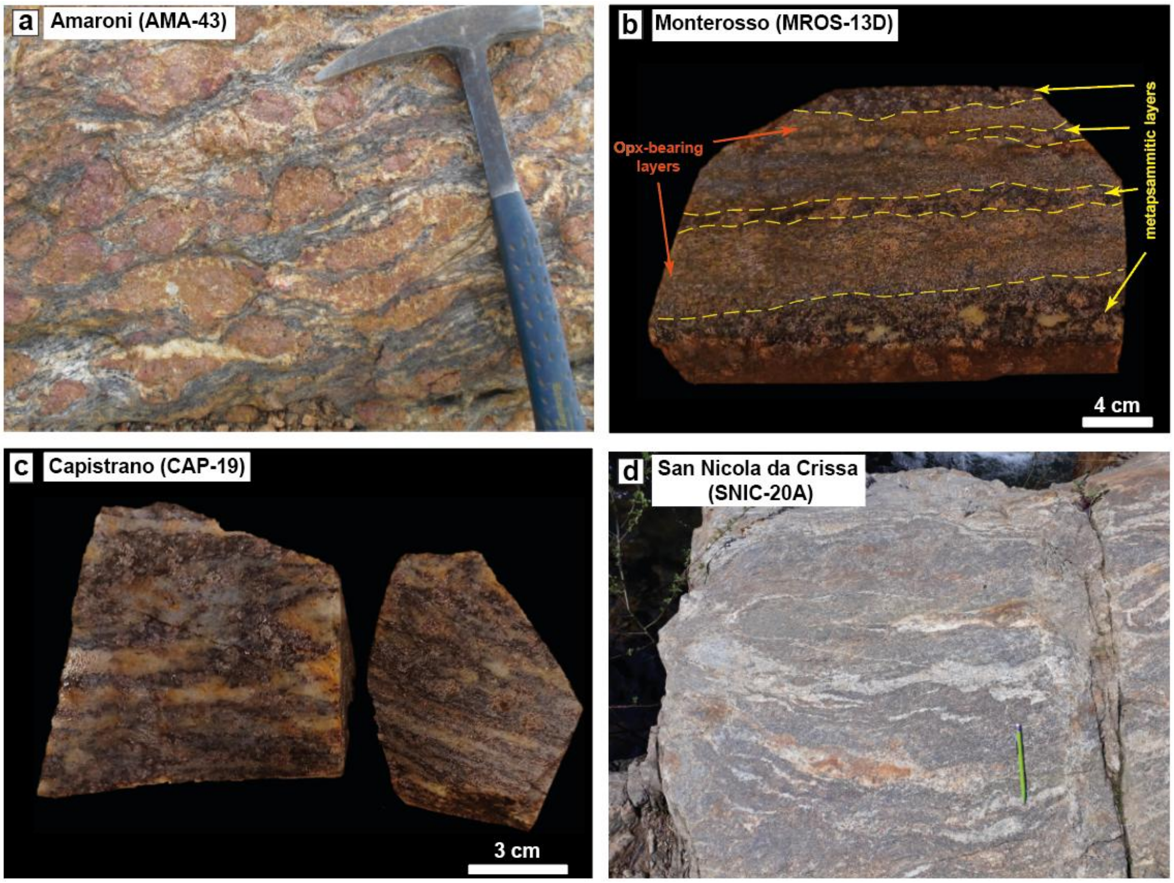

Figure S-5 Outcrop and macroscopic views of representative samples selected from the Metapelite Unit. **(a)** Outcrop of AMA-43 migmatitic paragneiss with giant garnets showing a strong restitic character. **(b)** MROS-13D composite gneiss with alternating metapsammitic and orthopyroxene-bearing layers. **(c)** CAP-19 migmatitic paragneiss. **(d)** SNIC-20A migmatitic paragneiss.

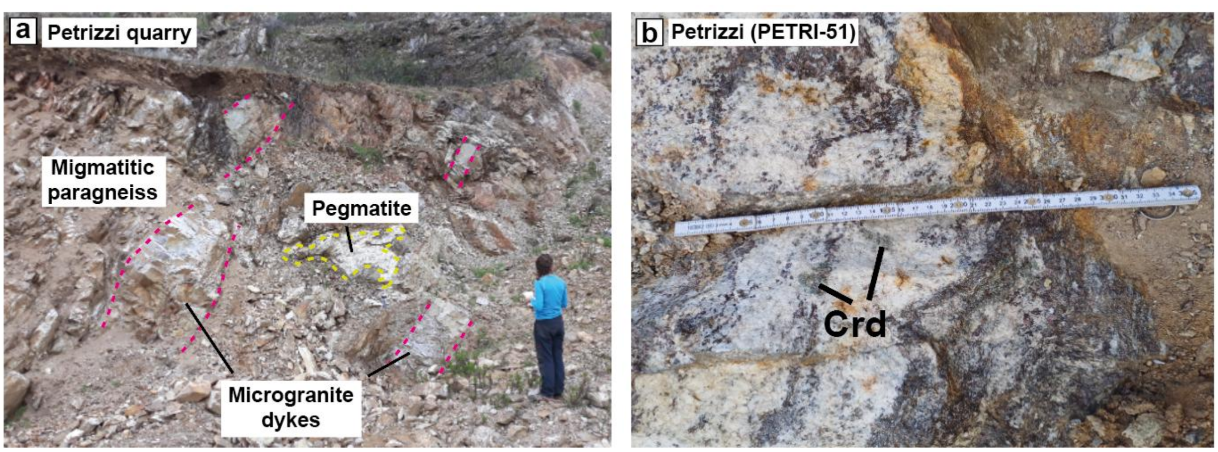

Figure S-6 **(a)** Exposure of the complex outcrops typical of the Migmatitic Border Zone in the Petrizzi quarry, showing migmatitic paragneisses cross-cut by late pegmatite and microgranite dykes. **(b)** Macroscopic view of PETRI-51 migmatitic paragneiss displaying large cordierite crystals.

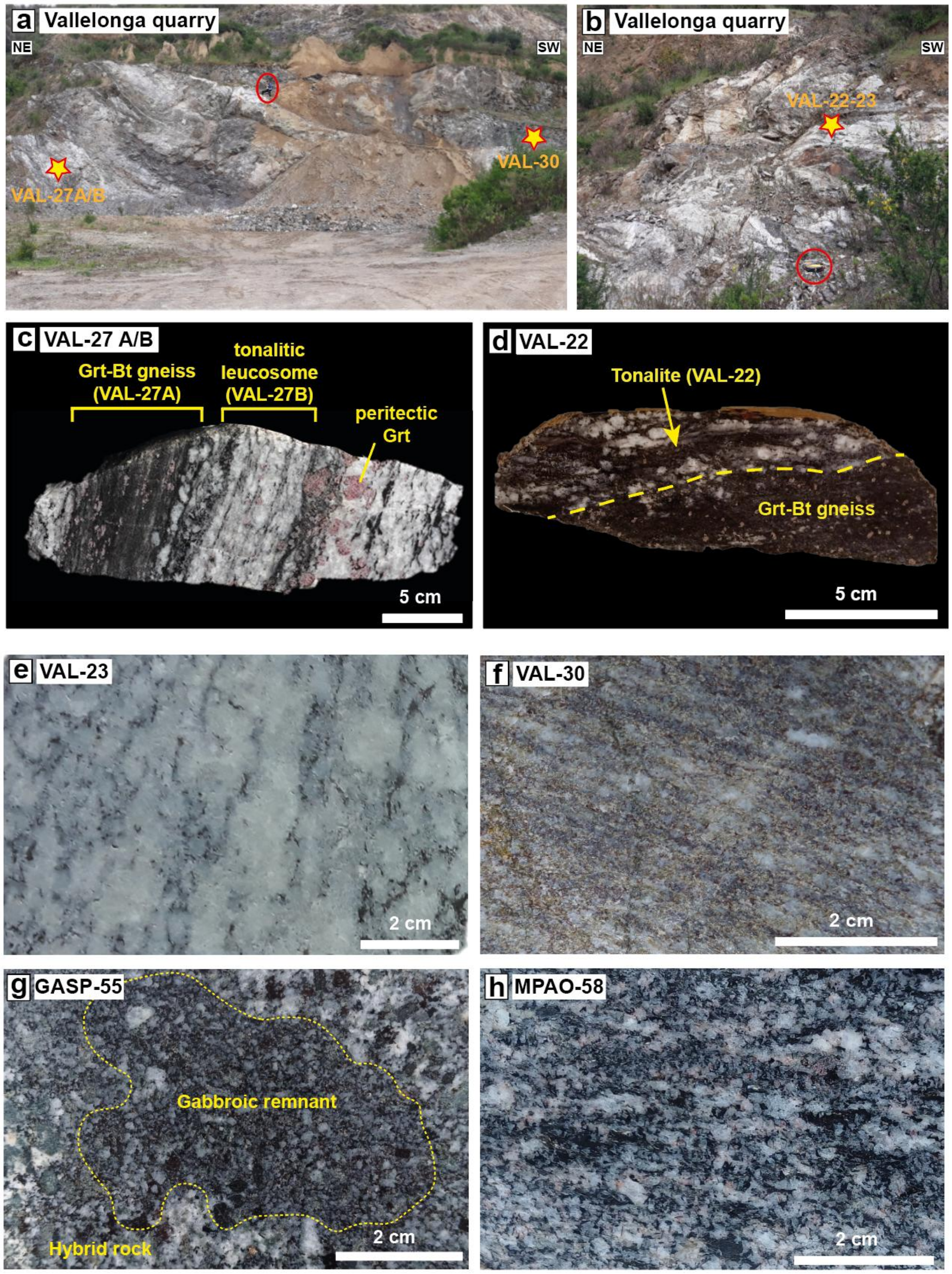

Figure S-7 **(a-b)** Exposure of the complex outcrops typical of the Migmatitic Border Zone in the Vallelonga quarry, showing an anatectic garnet-biotite gneiss interspersed by various igneous rocks including tonalite, monzogranite, and two-mica granite. The circled person in **(a)** and the circled bag in **(b)** give the scale. **(c)** Macroscopic view of VAL-27 diatexite consisting of garnet-biotite gneiss mesosomes (VAL-27A) and tonalitic leucosomes (VAL-27B). **(d)** Foliated amphibole-garnet tonalite (VAL-22) in contact with the garnet-biotite gneiss. **(e)** Sheared monzogranitic intrusion of the Vallelonga quarry (VAL-23). **(f)** Strongly foliated orthopyroxene-cummingtonite mafic rock (VAL-30). **(g)** Hybrid amphibole-bearing mafic rock in Gasperina showing remnants of the original gabbro (GASP-55). **(h)** Foliated garnet-bearing tonalite (MPAO-58).

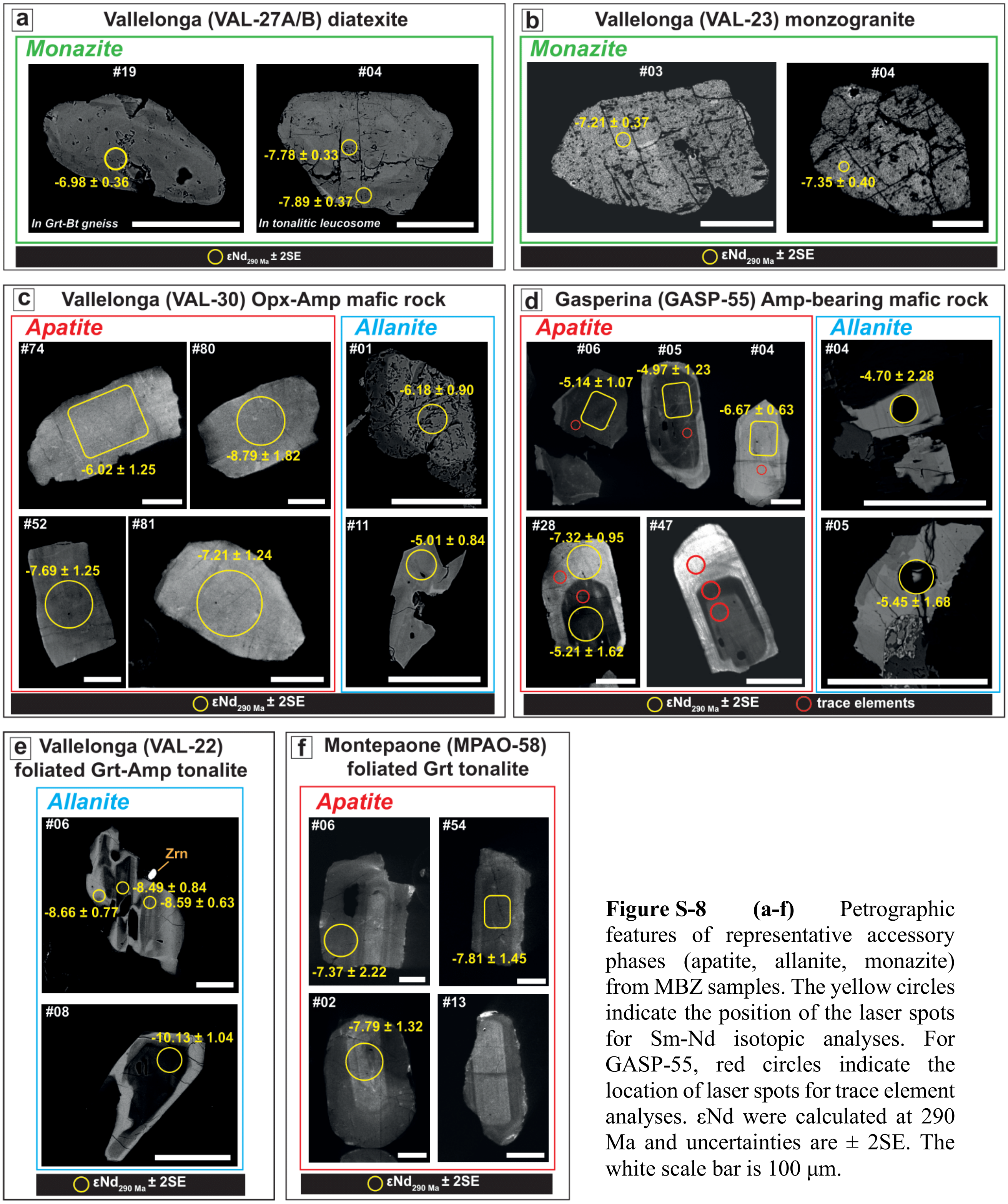

Figure S-8 **(a-f)** Petrographic features of representative accessory phases (apatite, allanite, monazite) from MBZ samples. The yellow circles indicate the position of the laser spots for Sm-Nd isotopic analyses. For GASP-55, red circles indicate the location of laser spots for trace element analyses. εNd were calculated at 290 Ma and uncertainties are ± 2SE. The white scale bar is 100 μm.

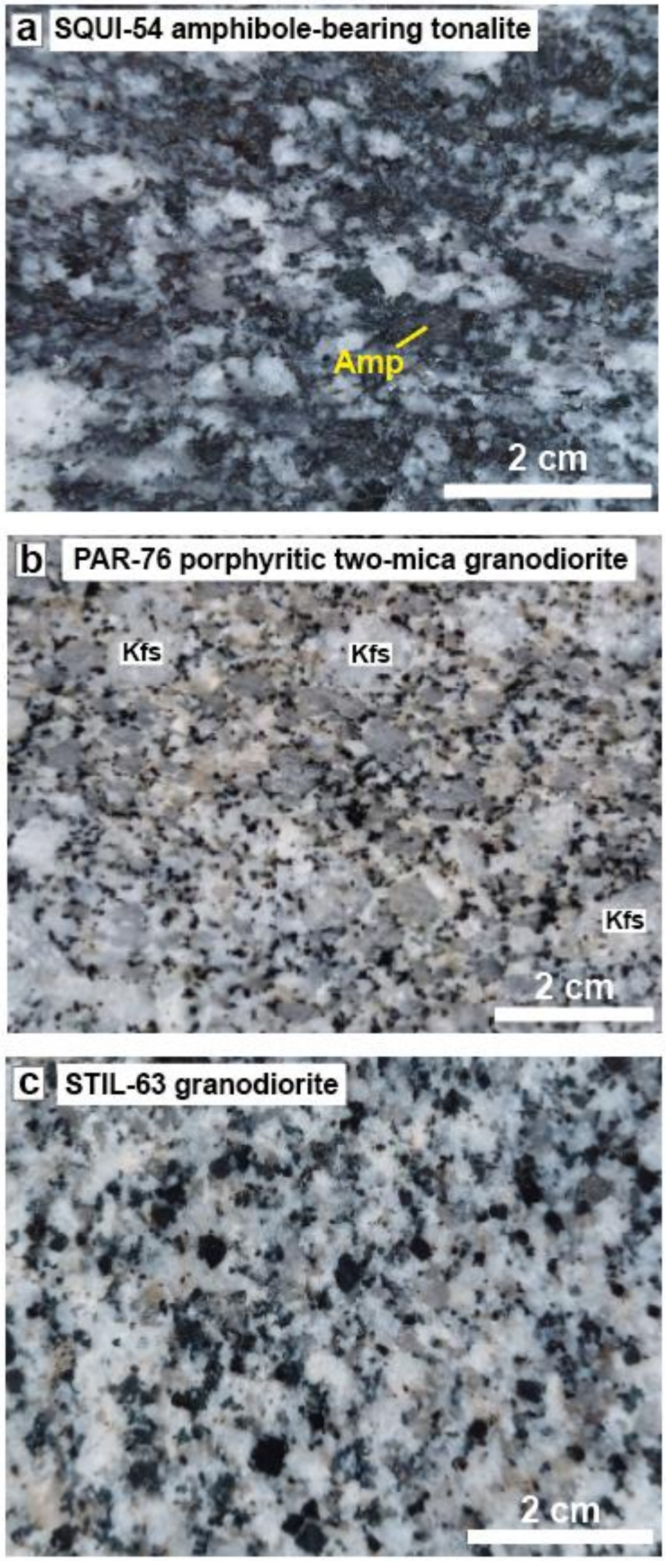

Figure S-9 Mesoscopic appearance of the middle crust granitoids: **(a)** foliated amphibole-bearing tonalite (SQUI-54); **(b)** two-mica granodiorite exhibiting a porphyritic texture with K-feldspar megacrysts (PAR-76) and **(c)** biotite granodiorite (STIL-63).

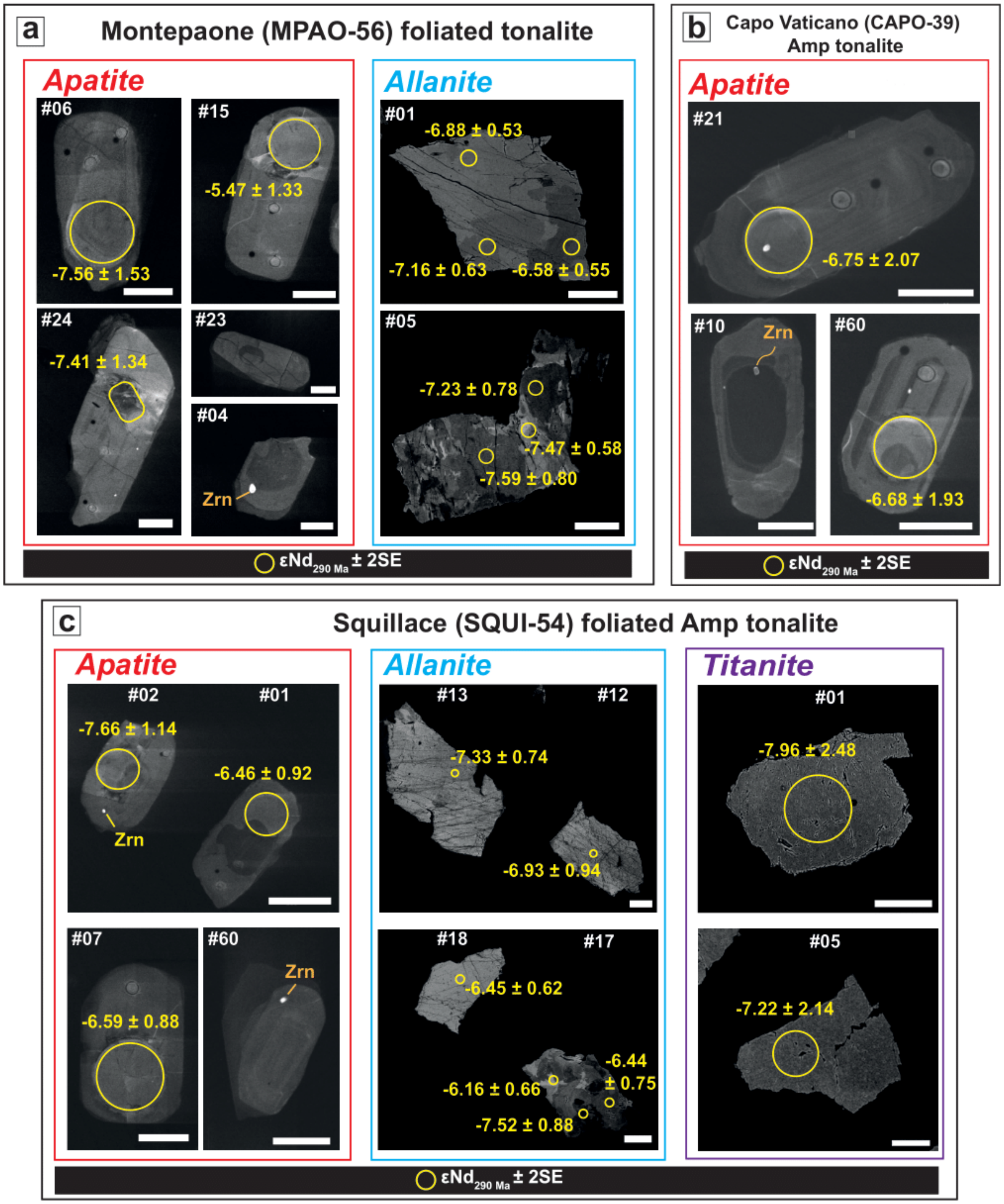

Figure S-10 **(a-c)** Petrographic features of representative accessory phases (apatite, allanite, and titanite) from the selected samples of the tonalite unit. The yellow circles indicate the position of the laser spots for Sm-Nd isotopic analyses. εNd were calculated at 290 Ma and uncertainties are ± 2SE. The white scale bar is 100 µm.

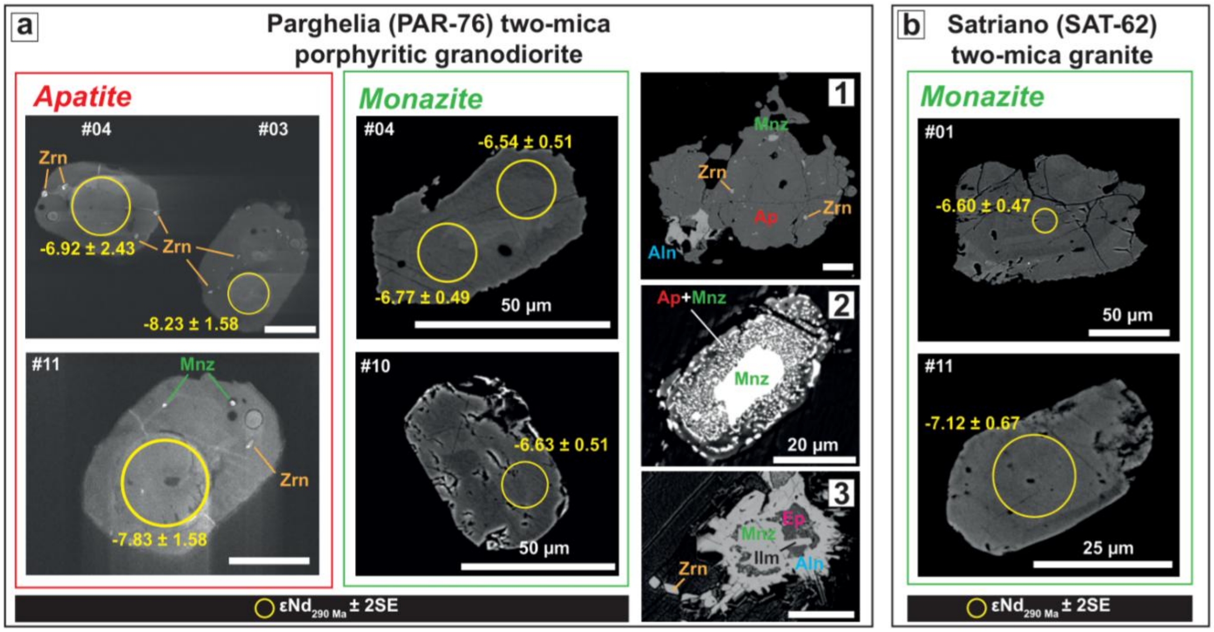

Figure S-11 **(a-b)** Petrographic features of representative accessory phases (apatite and monazite) from the selected samples of the two-mica granite/granodiorite unit. **(a1-3)** Details on the relationships between accessory minerals in PAR-76 two-mica porphyritic granodiorite. The yellow circles indicate the position of the laser spots for Sm-Nd isotopic analyses. εNd were calculated at 290 Ma and uncertainties are ± 2SE. The white scale bar, unless otherwise stated, is 100 µm.

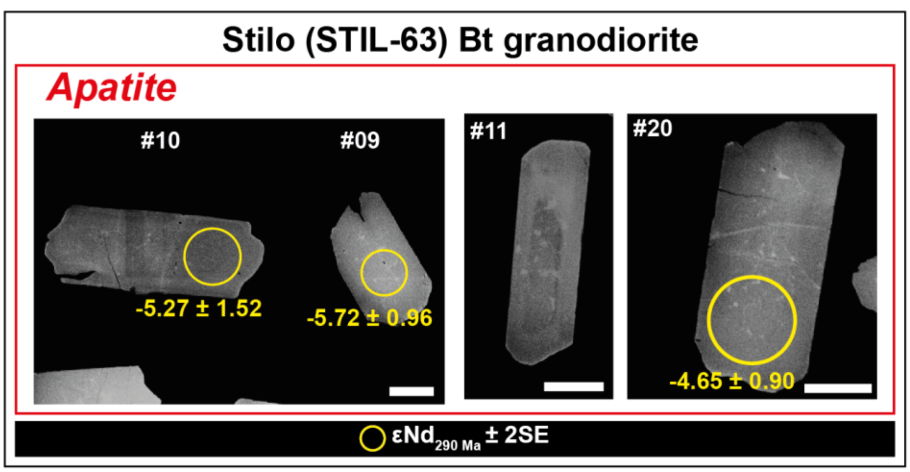

Figure S-12 CL images of apatite from STIL-63 biotite granodiorite. The yellow circles indicate the position of the laser spots for Sm-Nd isotopic analyses. εNd were calculated at 290 Ma and uncertainties are ± 2SE. The white scale bar is 100 µm.

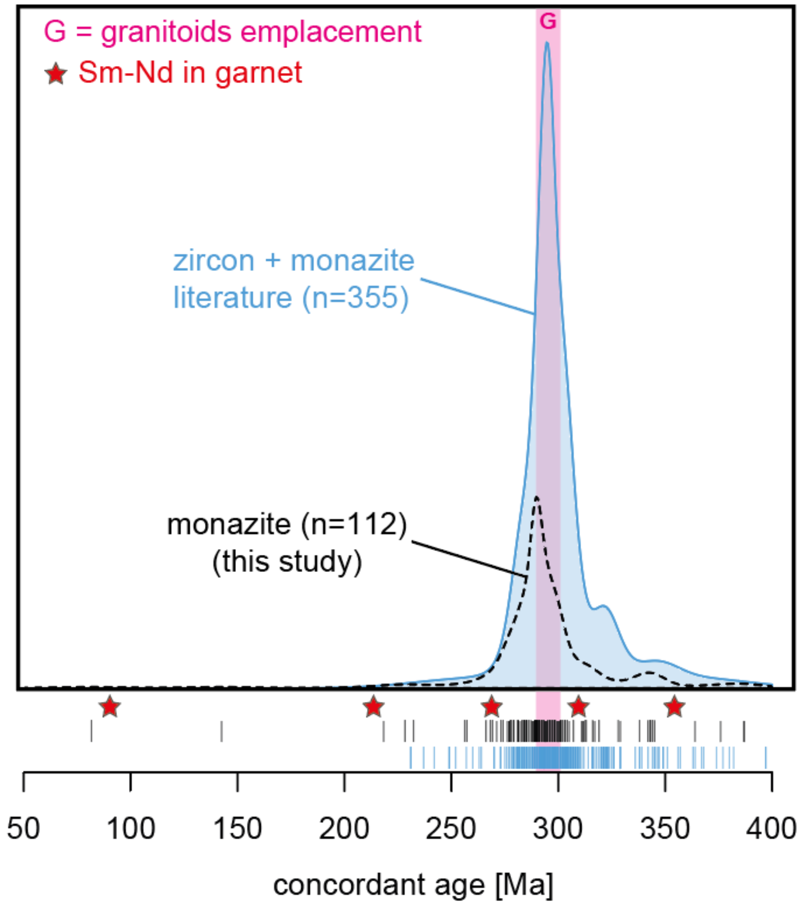

Figure S-13 Kernel Density Estimation (KDE) diagram of concordant monazite U–Pb dates from lower-crustal and mid-crustal igneous samples of the Serre Massif–Capo Vaticano area (black dotted curve; Biget, 2024), compared with concordant zircon and monazite U-Pb dates from granitoids and migmatites reported in the literature (blue curve; Schenk, 1980; Graessner *et al.*, 2000; Micheletti *et al.*, 2008; Fornelli *et al.*, 2011; Langone *et al.*, 2014; Fiannacca *et al.*, 2017). Garnet Sm-Nd dates are also shown (red stars; Duchene *et al.*, 2013) as well as the timing of mid-crustal granitoid emplacement (*e.g.*, Langone *et al.*, 2014; Fiannacca *et al.*, 2017).

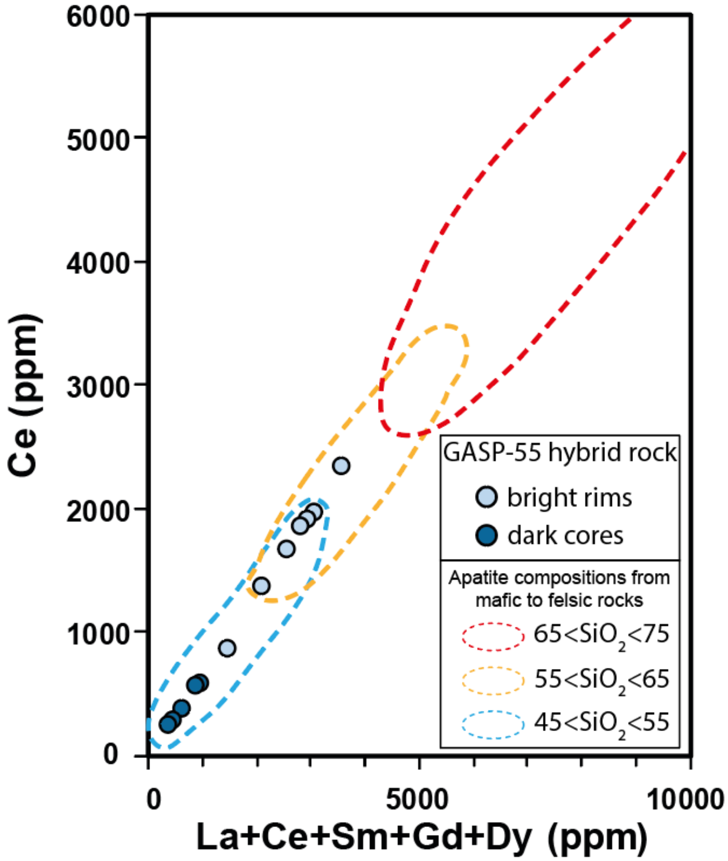

Figure S-14 GASP-55 apatite plotted in the diagram of Xu *et al.* (2024) allowing a comparison with apatite crystallised from mafic to felsic rocks (SiO_2 contents ranging from 45 to 75 wt.%).

4. Supplementary Tables

Table S-1 Summary of the rock-forming minerals and accessory phases for the lower crust samples.

	Unit	**Granulite Unit**					
	Sample	CUR-07	CUR-01A	CUR-03	ZAP-11	CUR-05A	CUR-02
	Locality	Acconia quarry (Curinga)	Turrino quarry (Curinga)	Turrino quarry (Curinga)	Zappaterra	Acconia quarry (Curinga)	Turrino quarry (Curinga)
	Latitude (°N)	38.8439	38.8218	38.8215	38.7688	38.8439	38.822
	Longitude (°E)	16.2858	16.2955	16.2967	16.333	16.2858	16.2954
	Rock type	Amp (meta)gabbro	Mafic granulite	Mafic granulite	Mafic granulite	Felsic granulite	Felsic granulite
Rock-forming minerals	**Qz**			(X)	(X)	(X)	X
	Pl	X	X	X	X	X	X
	Kfs			X	(X)	X	X
	Bt		X	X	X	X	X
	Grt					X	X
	Sil						
	Crd						
	Hbl	X	X		X		
	Px	Cpx	Cpx	Opx (+Cpx)	Opx+Cpx		
	other					Chl, Ep	
Accessories	**Ap**	X	X	X	X	(X)	X
	Mnz			(X)		X	X
	Zrn	X	X	X	X	X	X
	Aln			X	(X)	(X)	
	Xtm			(X)			
	Ilm	X	X	(X)	X		X
	Rt					X	X
	Ox	X	X		X	X	
	Sulf	X	X	X	X	(X)	X

Table S-1 Continued.

	Unit	**Metapelite Unit**						**Migmatitic Border Zone**
	Sample	AMA-43	MROS-13A	MROS-13D	MROS-16	CAP-19	SNIC-20A	PETRI-51
	Locality	Amaroni	Monterosso Calabro	Monterosso Calabro	Monterosso Calabro	Capistrano	San Nicola da Crissa	Petrizzi
	Latitude (°N)	38.7787	38.7250	38.7250	38.7094	38.6869	38.6665	38.7025
	Longitude (°E)	16.4280	16.2987	16.2987	16.2903	16.2951	16.2928	16.4455
	Rock type	migmatitic paragneiss (highly restitic)	migmatitic paragneiss (metapsammite)	Composite gneiss with Opx layers	migmatitic paragneiss	migmatitic paragneiss	migmatitic paragneiss	migmatitic paragneiss
Rock-forming minerals	**Qz**	X	X	X	X	X	X	X
	Pl	X	X	X	X	X	X	X
	Kfs	X			X	X		
	Bt	X	X	X	X	X	X	X
	Grt	X	X	X	X	X	X	X
	Sil	X			X	X	X	X
	Crd					X	(X)	X
	Hbl							
	Px			Opx				
	Others							Cb, And
Accessories	**Ap**			X		(X)	X	X
	Mnz	X	X	X	X	X	X	X
	Zrn	X	X	X	X	X	X	X
	Aln							
	Xtm						(X)	(X)
	Ilm	X	X	X	X	X	X	X
	Rt	X	X	(X)	X	X	(X)	(X)
	Ox	X			X	X	X	X
	Sulf		X	X		X	X	X

Table S-2 Mineralogical content summary (rock-forming and accessory minerals) for the studied igneous sample, ordered according to their approximate structural position within the crustal section. For rock-forming minerals, the number in brackets is the modal proportion (in %) of each phase estimated with images processed on Aztec and ImageJ softwares (Schneider *et al.*, 2012). The two samples highlighted in yellow come from the CVP area. Mineral abbreviations are from Whitney and Evans (2010).

Samples name	Locality	Unit	Coordinates	Type	Rock-forming minerals	Accessory minerals
VAL-22	Vallelonga	MBZ	38.6543 °N 16.2789 °E	Foliated Grt-Amp tonalite	Bt (37), Pl (31), Qz (17), Grt (4), Hbl (2), Cum(1)	Ilm, Ap, Zrn, Aln, Mnz
VAL-23	Vallelonga		38.6543 °N 16.2789 °E	Sheared monzogranite	Kfs (37), Qz (34), Pl (25), Bt (4), Ms (<1%)	Ilm, Mnz, Zrn, Ap
VAL-27A	Vallelonga		38.6543 °N 16.2789 °E	Diatexite: Grt-Bt gneiss mesosome	Pl (41), Qz (29), Bt (28), Grt (2)	Ilm, Mnz, Zrn, (Xtm)
VAL-27B	Vallelonga		38.6543 °N 16.2789 °E	Diatexite: Tonalitic leucosome	Pl (57), Qz (21), Bt (20), Grt(2)	Ilm, Mnz, Zrn
VAL-30	Vallelonga		38.6543 °N 16.2789 °E	Foliated Opx-Cum mafic rock	Pl (57), Cum (19), Bt (14), Opx (8), Qz (2)	Ilm, Ap, Aln, Zrn
GASP-55	Gasperina		38.7447 °N 16.5082 °E	Hbl-Cum mafic rock	Pl (53), Hbl (21), Cum (19), Bt (5), Qz (2)	Ilm, Ap, Zrn, Aln
MPAO-58	Montepaone		38.7260 °N 16.4794 °E	Foliated Grt-bearing tonalite	Pl (50), Qz (26), Bt (22), Grt (2), Chl (<1%)	Ilm, Ap, Zrn
MPAO-56	Montepaone	Middle crust granitoids	38.7228 °N 16.4902 °E	Foliated tonalite	Pl (59), Qz (23), Bt (18), Ep (<1%)	Ilm, Ap, Zrn, Aln, (Ttn)
SQUI-54	Squillace		38.7643 °N 16.5166 °E	Foliated Amp tonalite	Pl (48), Bt (23), Qz (23), Hbl (5)	Ilm, Ap, Zrn, Ttn, Aln
CAPO-39	Capo Vaticano		38.6222 °N 15.8280 °E	Amp tonalite	Pl (47), Qz (34), Bt (11), Kfs (5), Amp (1), Chl (1), Ep (<1%)	Ttn, Ap, Zrn
PAR-76	Parghelia		38.6855 °N 15.9210 °E	Ms-Bt porphyritic granodiorite	Pl (32), Qz (30), Kfs (25), Bt (8), Ms (5)	Zrn, Ilm, Ap, Mnz, Aln, Ttn
SAT-62	Satriano		38.6616 °N 16.5019 °E	Ms-Bt granite	Pl (39), Qz (32), Kfs (20), Ms (7), Bt (2)	Ap, Ilm, Zrn, Aln, Mnz, (Ttn, Xtm)
STIL-63	Stilo		38.4682 °N 16.4090 °E	Bt granodiorite	Pl (46), Qz (31), Bt (11), Kfs (11), Chl (1), Ep (<1%)	Ap, Ttn, Zrn, Ilm, (Aln)

Table S-3 Whole rock Sm-Nd isotopic compositions.

Table S-4 Nd isotopic composition of unknown apatite, allanite, monazite and titanite.

Table S-5 Durango apatite, Connecticut allanite, STK monazite and MKED1 titanite values used for further normalisation on unknowns and to correct from instrumental drift (primary standard).

Table S-6 Tory Hill apatite, Gale allanite and Khan titanite values (secondary standard).

Table S-7 EPMA analytical results for Durango apatite standard.

Table S-8 EPMA and LA-ICP-MS analytical results for GASP-55 apatite.

Table S-9 LA-ICP-MS analytical results for international reference materials (NIST-612, Durango).

Tables S-3 to S-9 *are available for download as a single file (.xlsx) from the online version of this article at https://doi.org/10.7185/geochemlet.2602.* .

5. Supplementary Information References

Acquafredda, P., Fornelli, A., Paglionico, A., Piccarreta, G. (2006) Petrological evidence for crustal thickening and extension in the Serre granulite terrane (Calabria, southern Italy). *Geological Magazine* 143(2), 145-163. https://doi.org/10.1017/s0016756805001482

Acquafredda, P., Fornelli, A., Piccarreta, G., Pascazio, A. (2008) Multi-stage dehydration– decompression in the metagabbros from the lower crustal rocks of the Serre (southern Calabria, Italy). *Geological Magazine* 145(3), 397-411. https://doi.org/10.1017/s001675680700430x

Biget, T. (2024) Processus de fusion partielle et différenciation crustale : nouvelles contraintes apportées par l'étude des minéraux accessoires et le système isotopique Sm-Nd. PhD thesis. University Clermont-Auvergne (UCA), France. 261 pp.

Bouvier, A., Vervoort, J.D., Patchett, P.J. (2008) The Lu–Hf and Sm–Nd isotopic composition of CHUR: Constraints from unequilibrated chondrites and implications for the bulk composition of terrestrial planets. *Earth and Planetary Science Letters* 273, 48–57. https://doi.org/10.1016/j.epsl.2008.06.010

Brandt, S., Schenk, V. (2020) Metamorphic Response to Alpine Thrusting of a Crustal-scale Basement Nappe in Southern Calabria (Italy), *Journal of Petrology* 61, 11-12. https://doi.org/10.1093/petrology/egaa063

Caggianelli, A., Del Moro, A., Paglionico, A., Piccarreta, G., Pinarelli, L., Rottura, A. (1991) Lower crustal granite genesis connected with chemical fractionation in the continental crust of Calabria (Southern Italy). *European Journal of Mineralogy* 3, 159–180.

Caggianelli, A., Prosser, G., Rottura, A. (2000) Thermal history vs. fabric anisotropy in gran itoids emplaced at different crustal levels: an example from Calabria, southern Italy. *Terra Nova* 12, 109–116. https://doi.org/10.1046/j.1365-3121.2000.123280.x

Caggianelli, A., Prosser, G., Festa, V., Langone, A., Spiess, R. (2013) From the upper to the lower continental crust exposed in Calabria. *Geological Field Trips* 5. 49 pp. https://doi.org/10.3301/gft.2013.02

Chauvel, C., Bureau, S., Poggi, C. (2010) Comprehensive Chemical and Isotopic Analyses of Basalt and Sediment Reference Materials. *Geostandards and Geoanalytical Research* 35(1), 125–143. https://doi.org/10.1111/j.1751-908X.2010.00086.x

Doucelance, R., Bruand, E., Matte, S., Bosq, C., Auclair, D., Gannoun, A.-M. (2020) In-situ determination of Nd isotope ratios in apatite by LA-MC-ICPMS: challenges and limitations. *Chemical Geology* 119740. https://doi.org/10.1016/j.chemgeo.2020.119740 .

Duchene, S., Fornelli, A., Micheletti, F., Piccarreta, G. (2013) Sm-Nd chronology of porphyroblastic garnets from granulite facies metabasic rocks in Calabria (Southern Italy): inferences for preserved isotopic memory and resetting. *Mineralogy and Petrology* 107, 539–551. https://doi.org/10.1007/s00710-012-0229-3

Ellis, D., Hiroi, Y. (1997) Secondary siderite-oxide-sulphide and carbonate-andalusite assemblages in cordierite granulites from Sri Lanka: post-granulite facies fluid evolution during uplift. *Contributions to Mineralogy and Petrology* 127, 315–335. https://doi.org/10.1007/s004100050283

Festa, V., Messina, A., Paglionico, A., Piccarreta, G. Rottura, A. (2004) Pre-Triassic history recorded in the Calabria-Peloritani segment of the Alpine chain, Southern Italy. An overview. In: Castelli D., Cesare B. (Eds.): A showcase of the Italian research in metamorphic petrology. *Periodico di Mineralogia*, 73/2 (Spec. Issue), 57–71.

Festa, V., Caggianelli, A., Langone, A., Prosser, G. (2013) Time–space relationships among structural and metamorphic aureoles related to granite emplacement: a case study from the Serre Massif (southern Italy). *Geological Magazine* 150, 441–454. https://doi:10.1017/S0016756812000714

Festa, V., Cicala, M., Tursi, F. (2020) The Curinga–Girifalco line in the framework of the tectonic evolution of the remnant Alpine chain in Calabria (southern Italy). *International Journal of Earth Sciences* 109, 2583-2598. https://doi.org/10.1007/s00531-020-01918-5

Festa, V., Spiess, R., Tursi, F. (2024) Garnet coalescence clogs melt extraction channels in migmatite. *Lithos* 472–473, 107581. https://doi.org/10.1016/j.lithos.2024.107581

Fiannacca, P., Cirrincione, R., Bonanno, F., Carciotto, M.M. (2015) Source-inherited compositional diversity in granite batholiths: the geochemical message of Late Paleozoic intrusive magmatism in central Calabria (southern Italy). *Lithos* 236–237, 123–140. https://doi.org/10.1016/j.lithos.2015.09.003

Fiannacca, P., Williams, I.S., Cirrincione, R. (2017) Timescales and mechanisms of batholith construction: Constraints from zircon oxygen isotopes and geochronology of the late Variscan Serre Batholith (Calabria, southern Italy). *Lithos* 277, 302–314. https://doi.org/10.1016/j.lithos.2016.06.011

Fiannacca, P., Cirrincione, R., Fazio, E., Russo, D. (2024) Calabria coast to coast: a nearly complete cross-section of continental crust, with a 13 km-thick late Variscan batholith. *Geological Field Trips and Maps* 16 (2.4). 84 pp. https://doi.org/10.3301/GFT.2024.09.

Fisher, C.M., McFarlane, C.R.M., Hanchar, J.M., Schmitz, M.D., Sylvester, P.J., Lam, R., Longerich, H.P. (2011) Sm–Nd isotope systematics by laser ablation-multicollector inductively coupled plasma mass spectrometry: Methods and potential natural and synthetic reference materials. *Chemical Geology* 284, 1–20. https://doi.org/10.1016/j.chemgeo.2011.01.012

Fisher, C.M., Bauer, A.M., Luo, Y., Sarkar, C., Hanchar, J.M., Vervoort, J.D., Tapster, S.R., Horstwood, M., Pearson, D.G. (2020) Laser ablation split-stream analysis of the Sm–Nd and U-Pb isotope compositions of monazite, titanite, and apatite – Improvements, potential reference materials, and application to the Archean Saglek Block gneisses. *Chemical Geology* 539, 119493. https://doi.org/10.1016/j.chemgeo.2020.119493

Fornelli, A., Piccarreta, G., Del Moro, A., Acquafredda, P. (2002) Multi-stage melting in the lower crust of the Serre (southern Italy). *Journal of Petrology* 43, 2191–2217. https://doi.org/10.1093/petrology/43.12.2191.

Fornelli, A., Langone, A., Micheletti, F., Piccarreta, G. (2011) Time and duration of Variscan high temperature metamorphic processes in the south European Variscides: constraints from U–Pb chronology and trace element chemistry of zircon. *Mineralogy and Petrology* 103, 101–122. https://doi.org/10.1007/s00710-011-0156-8.

Fornelli, A., Pascazio, A., Piccarreta, G. (2012) Diachronic and different metamorphic evolution in the fossil Variscan lower crust of Calabria. *International Journal of Earth Sciences* 101, 1191- 1207. https://doi.org/10.1007/s00531-011-0721-8.

Fornelli, A., Festa, V., Micheletti, F., Spiess, R., Tursi, F. (2020) Building an orogen: Review of U-Pb zircon ages from the Calabria Peloritani terrane to constrain the timing of the southern Variscan belt. *Mineral* 10, 944. https://doi.org/10.3390/min10110944

Garçon, M., Boyet, M., Carlson, R.W., Horan, M.F., Auclair, D., Mock, T.D. (2018) Factors influencing the precision and accuracy of Nd isotope measurements by thermal ionization mass spectrometry. *Chemical Geology* 476, 493–514. https://doi.org/10.1016/j.chemgeo.2017.12.003

Graessner, T., Schenk, V., Brocker, M., Mezger, K. (2000) Geochronological constraints on the timing of granitoid magmatism, metamorphism and post- metamorphic cooling in the Hercynian crustal cross-section of Calabria. *Journal of Metamorphic Geology* 18, 409–421. https://doi.org/10.1046/j.1525-1314.2000.00267.x

Griffin, W.L., Powell, W.J., Pearson, N.J., O'Reilly, S.Y. (2008) GLITTER: data reduction software for laser ablation ICP-MS. In: Sylvester, P. (Ed.) *Laser Ablation–ICP–MS in the Earth Sciences.* Mineralogical Association of Canada Short Course Series 40, 204–207.

Ickert R. (2013) Algorithms for estimating uncertainties in initial radiogenic isotope ratios and model ages. *Chemical Geology* 340, 131–188. http://dx.doi.org/10.1016/j.chemgeo.2013.01.001

Jochum, K.P., Willbold, M., Raczek, I., Stoll, B., Herwig, K (2005) Chemical characterisation of the USGS reference glasses GSA-1G,GSC-1G, GSD-1G, GSE-1G, BCR-2G, BHVO-2G and BIR-1G using EPMA, ID-TIMS, ID-ICP-MS and LA-ICP-MS. *Geostandards and Geoanalytical Research* 29, 285–302. https://doi.org/10.1111/j.1751-908X.2005.tb00901.x

Langone, S., Caggianelli, A., Festa, V., Prosser, G. (2014) Time constraints on the building of the Serre batholith: consequences for the thermal evolution of the hercynian continental crust exposed in Calabria (Southern Italy). *Journal of Geology* 122, 183–199. https://doi.org/10.1086/675227

Lugmair, G.W., Marti, K. (1978) Lunar initial 143Nd/144Nd differential evolution of lunar crust and mantle. *Earth and Planetary Science Letters* 39, 349–357. https://doi.org/ 10.1016/0012-821X(78)90021-3

Marks, M.A., Wenzel, T., Whitehouse, M.J., Loose, M., Zack, T., Barth, M., Worgard, L., Krasz, V., Nelson Eby, G., Stosnach, H., Markl, G. (2012) The volatile inventory (F, cl, Br, S, C) of magmatic apatite: An integrated analytical approach. *Chemical Geology* 291, 241–255. https://doi.org/10.1016/j.chemgeo.2011.10.026

Micheletti, F., Fornelli, A., Piccarreta, G., Barbey, P., Tiepolo, M. (2008) The basement of Calabria (southern Italy) within the context of the southern European Variscides: LA-ICPMS and SIMS U–Pb zircon study. *Lithos* 104, 1-11. https://doi.org/10.1016/j.lithos.2007.11.003

Pin, C., Briot, D., Bassin, C.P., Poitrasson, F. (1994) Concomitant separation of strontium and samarium-neodymium for isotopic analysis in silicate samples, based on specific extraction chromatography. *Analytica Chimica Acta* 298 (2), 209–217. https://doi.org/10.1016/0003-2670(94)00274-6

Pyle, J.M., Spear, F.S., Wark, D.A. (2002) Electron microprobe analysis of REE in apatite, monazite and xenotime: Protocols and pitfalls. *Reviews in Mineralogy and Geochemistry* 48, 337–362. https://doi.org/10.2138/rmg.2002.48.8

Sawyer, E.W. (2008) Atlas of migmatites. The Canadian Mineralogist Special Publication 9. NRC Research Press, Ottawa, Ontario. https://doi.org/10.1139/9780660197876

Schenk, V. (1980) U-Pb and Rb-Sr radiometric dates and their correlation with metamorphic events in the granulite–facies basement of the Serre, Southern Calabria (Italy). *Contributions to Mineralogy and Petrology* 73, 23–38. https://doi.org/10.1007/bf00376258

Schenk, V. (1984) Petrology of felsic granulites, metapelites, metabasics, ultramafics and metacarbonates from southern Calabria (Italy): prograde metamorphism, uplift and cooling of a former lower crust. *Journal of Petrology* 25, 255–298. https://doi.org/10.1093/petrology/25.1.255

Schenk, V. (1990) The exposed crustal cross section of southern Calabria, Italy: Structure and evolution of a segment of hercynian crust. In: Salisbury, M.H., Fountain, D.M. (Eds.) Exposed Cross-Sections of the Continental Crust. NATO ASI Series 317. Springer, Dordrecht, 21-42. https://doi.org/10.1007/978-94-009-0675-4_2.

Schneider, C.A., Rasband, W.S., Eliceiri, K.W. (2012) NIH Image to ImageJ: 25 years of image analysis. *Nature Methods* 9, 671–675. https://doi.org/10.1038/nmeth.2089.

Schulz, B. (2021) Monazite Microstructures and Their Interpretation in Petrochronology. *Frontiers of Earth Science* 9, 668566. https://doi: 10.3389/feart.2021.668566.

Spandler, C., Hammerli, J., Sha, P., Hilbert-wolf, H., Hu, Y., Roberts, E., Schmitz, M. (2016) MKED1: a new titanite standard for in situ analysis of Sm–Nd isotopes and U–Pb geochronology. *Chemical Geology* 425, 110–126. https://doi.org/10.1016/j.chemgeo.2016.01.002.

Varga, J., Raimondo, T., Daczko, N.R., Adam, J. (2020) Experimental alteration of monazite in granitic melt: variable U–Th–Pb and REE mobility during melt-mediated coupled dissolution–precipitation. *Chemical Geology* 544, 119602. https://doi.org/10.1016/j.chemgeo.2020.119602

Van Achterbergh, E., Ryan, C.G., Jackson, S.E., Griffin, W.L. (2001) Data reduction software for LA-ICP-MS. In: Sylvester, P. (Ed.) Laser-Ablation-ICPMS in the Earth Sciences: Principles and Applications. Short Course, vol. 29. Mineralogical Association of Canada, 239–243.

Wang, D., Shirey, S.B., Carlson, R.W., Fisher, C.M., Kemp, A.I., Bickford, M.E. (2022) Comparative Sm-Nd isotope behavior of accessory minerals: reconstructing the Sm-Nd isotope evolution of early Archean rocks. *Geochimica Cosmochimica Acta* 318, 190–212. https://doi.org/10.1016/j.gca.2021.11.031

Wasserburg, G., Jacobsen, S., DePaolo, D., McCulloch, M., Wen, T. (1981) Precise determination of Sm/Nd ratios, Sm and Nd isotopic abundances in standard solutions. *Geochimica Cosmochimica Acta* 45, 2311–2323. https://doi.org/10.1016/0016-7037(81)90085-5

Whitney, D.L., Evans, B.W. (2010) Abbreviations for names of rock-forming minerals, *American Mineralogist* 95, 185–187. https://doi.org/10.2138/am.2010.3371

Xu, L., Yang, J., Ni, Q., Yang, Y., Hu, Z., Liu, Y., Wu, Y., Luo, T., Hu, S. (2018) Determination of Sm-Nd isotopic compositions in fifteen geological materials using laser ablation MC-ICP-MS and application to monazite geochronology of metasedimentary rock in the North China Craton. *Geostandards and Geoanalytical Research* 42, 379-394. https://doi.org/10.1111/ggr.12210

Xu, J., Xia, X.-P., Wang, Q., Spencer, C.J., Zhang, L., Zhu, X. (2024) Apatite textures, elemental and isotopic compositions unmask the homogenizing process in silicic magma chambers. *Geophysical Research Letters* 51, e2023GL106646. https://doi. org/10.1029/2023GL106646